

④

TECHNICAL REPORT BRL-TR-3049

BRL

DTIC FILE COPY

AD-A218 824

PARALLEL COMPUTATION OF SUPERSONIC FLOWS USING
A THREE-DIMENSIONAL, ZONAL, NAVIER-STOKES CODE

N. R. PATEL
W. B. STUREK
G. A. SMITH

NOVEMBER 1989

APPROVED FOR PUBLIC RELEASE; DISTRIBUTION UNLIMITED.

U.S. ARMY LABORATORY COMMAND

BALLISTIC RESEARCH LABORATORY
ABERDEEN PROVING GROUND, MARYLAND

90 03 05 007

DESTRUCTION NOTICE

Destroy this report when it is no longer needed. DO NOT return it to the originator.

Additional copies of this report may be obtained from the National Technical Information Service, U.S. Department of Commerce, Springfield, VA 22161.

The findings of this report are not to be construed as an official Department of the Army position, unless so designated by other authorized documents.

The use of trade names or manufacturers' names in this report does not constitute indorsement of any commercial product.

UNCLASSIFIED

SECURITY CLASSIFICATION OF THIS PAGE

REPORT DOCUMENTATION PAGE				Form Approved OMB No. 0704-0188	
1a. REPORT SECURITY CLASSIFICATION UNCLASSIFIED			1b. RESTRICTIVE MARKINGS		
2a. SECURITY CLASSIFICATION AUTHORITY			3. DISTRIBUTION/AVAILABILITY OF REPORT Approved for public release, distribution unlimited.		
2b. DECLASSIFICATION/DOWNGRADING SCHEDULE					
4. PERFORMING ORGANIZATION REPORT NUMBER(S) BRL-TR-3049			5. MONITORING ORGANIZATION REPORT NUMBER(S)		
6a. NAME OF PERFORMING ORGANIZATION U.S. Army Ballistic Research Laboratory		6b. OFFICE SYMBOL (If applicable) SLCBR-LF	7a. NAME OF MONITORING ORGANIZATION		
6c. ADDRESS (City, State, and ZIP Code) Aberdeen Proving Ground, Maryland 21005-5066			7b. ADDRESS (City, State, and ZIP Code)		
8a. NAME OF FUNDING/SPONSORING ORGANIZATION		8b. OFFICE SYMBOL (If applicable)	9. PROCUREMENT INSTRUMENT IDENTIFICATION NUMBER		
8c. ADDRESS (City, State, and ZIP Code)			10. SOURCE OF FUNDING NUMBERS		
PROGRAM ELEMENT NO. 61102A		PROJECT NO. 1L161102AH43	TASK NO. 00	WORK UNIT ACCESSION NO. 001 AJ	
11. TITLE (Include Security Classification) PARALLEL COMPUTATION OF SUPERSONIC FLOWS USING A THREE DIMENSIONAL, ZONAL, NAVIER-STOKES CODE					
12. PERSONAL AUTHOR(S) PATEL, NISHEETH R., STUREK, WALTER B., and SMITH, GLENN A.					
13a. TYPE OF REPORT Technical Report		13b. TIME COVERED FROM _____ TO _____	14. DATE OF REPORT (Year, Month, Day)		15. PAGE COUNT 35
16. SUPPLEMENTARY NOTATION					
17. COSATI CODES			18. SUBJECT TERMS (Continue on reverse if necessary and identify by block number)		
FIELD 01	GROUP 01	SUB-GROUP	Parallel Computation: Projectile Aerodynamics		
			Navier-Stokes Zonal Grid		
			Supersonic Flow Supercomputers		
19. ABSTRACT (Continue on reverse if necessary and identify by block number) A three-dimensional, time marching, Navier-Stokes code has been developed to solve the flow field around complex geometries using a zonal grid frame-work. This report outlines the development of the new code and describes the application of the code to compute the flow field about a blunt-nosed, axisymmetric body shape. The code extends the computational efficiency of MacCormack's explicit method by incorporating a local variable time-stepping scheme and a new smoothing. Additionally, the code incorporates several features to enhance the coverage rate and minimize the size of the computational grid required for accurate solutions. The computational performance achieved through the efficient utilization of the vector and parallel architecture on the Cray 2 and the Cray Y-MP supercomputers is defined. Comparison of the computations with experimental measurements of surface pressure distribution and boundary layer velocity profiles are presented.					
20. DISTRIBUTION/AVAILABILITY OF ABSTRACT <input checked="" type="checkbox"/> UNCLASSIFIED/UNLIMITED <input type="checkbox"/> SAME AS RPT. <input type="checkbox"/> DTIC USERS			21. ABSTRACT SECURITY CLASSIFICATION UNCLASSIFIED		
22a. NAME OF RESPONSIBLE INDIVIDUAL Walter B. Sturek			22b. TELEPHONE (Include Area Code) (301) 278-4773		22c. OFFICE SYMBOL SLCBR-LF-C

INTENTIONALLY LEFT BLANK.

Acknowledgment

Cray Research Inc. provided time on their Cray Y-MP for this study. The performance measurement work benefited from collaboration with Mr. Regional Daniel of Cray Research. This contribution is gratefully acknowledged.

Accession For	
NTIS GRANT	<input checked="" type="checkbox"/>
DTIC TAB	<input type="checkbox"/>
Unannounced	<input type="checkbox"/>
Justification	
Form Approved by GSA	
Dist. 0-78	
Approved for Release	
Date	
Dist. 0-78	
A-1	



INTENTIONALLY LEFT BLANK.

Table of Contents

	<u>Page</u>
List of Figures	vii
I. INTRODUCTION	1
II. GOVERNING EQUATIONS	2
III. NUMERICAL METHOD	4
1. COMPUTATIONAL ALGORITHM	4
2. NUMERICAL DAMPING	5
3. ZONAL GRIDDING	6
4. BOUNDARY CONDITIONS AND TURBULENCE MODEL	7
IV. MODEL GEOMETRY AND EXPERIMENT	8
V. COMPUTATIONAL RESULTS	8
VI. PARALLEL IMPLEMENTATION AND PERFORMANCE	10
VII. CONCLUDING REMARKS	11
References	27
APPENDIX A: NON-REFLECTING OUTER BOUNDARY CONDITION	29

INTENTIONALLY LEFT BLANK.

List of Figures

<u>Figure</u>		<u>Page</u>
1	Schematic illustration of single grid-cell overlap.	12
2	Schematic of the model.	13
3	Body surface and pitch plane computational grid.	14
4	Pitch plane computational grid, nose region.	15
5	Wind tunnel spark shadowgraph of flow over blunt model, $M = 2.95$, $\alpha = 0.0^\circ$	16
6	Computational results, Mach contour in nose region, $\alpha = 0.0^\circ$	17
7	Surface pressure distribution, computation compared to experiment, $\alpha = 0.0^\circ$	18
8	u-velocity profile, computation compared to experiment, $\alpha = 0.0^\circ$, $X/D = 2.86, 4.65$ and 5.93	19
9	Wind tunnel spark shadowgraph of flow over blunt model, $M = 2.95$, $\alpha = 3.0^\circ$	20
10	Computational results, Mach contour in nose region, $\alpha = 3.0^\circ$	21
11	Surface pressure distribution, computation compared to experiment, $\alpha = 3.0^\circ$, wind and lee-side.	22
12	u-velocity profile, computation compared to experiment, $\alpha = 3.0^\circ$, $X/D = 2.86, 4.65$ and 5.93 , lee-side.	23
13	u-velocity profile, computation compared to experiment, $\alpha = 3.0^\circ$, $X/D = 2.86, 4.65$ and 5.93 , wind-side.	24
14	Speedup on Cray-2 - 3D microtasked code.	25
15	Speedup on Cray Y-MP - 3D zonal code.	26
A1	Non-reflection boundary condition.	31

INTENTIONALLY LEFT BLANK.

I. INTRODUCTION

Accurate prediction of the three-dimensional flow over a projectile is essential for obtaining aerodynamic design parameters such as body forces and moments. A bibliography and discussion of experimental and numerical work as applied to projectile aerodynamics has been reported by Sturek,¹ and Nietubicz and Sturek.² Although many design parameters can be calculated with acceptable accuracy for simple geometries, much remains to be done for projectile shapes which include such geometry features as flattened nose tips, rotating bands, undercuts, irregular base configurations and fins.

This report outlines the development of a three-dimensional Navier-Stokes code which uses explicit time-marching and zonal gridding. The development of this code was initiated in order to explore techniques for performing CFD computations utilizing the vector and parallel features of advanced computer architectures. The initial development was carried out for two-dimensional, axisymmetric flow.³

The results achieved, as reported in Reference 3, were sufficiently encouraging from the standpoint of computational efficiency and accuracy of the flow field predictions for highly complex flows to justify extension of the code to achieve a three-dimensional modeling capability. This code incorporates a fourth order dissipation and variable, local, time-stepping within MacCormack's⁴ predictor-corrector algorithm to accelerate the convergence. A non-reflecting outer boundary is implemented in order to reduce the total number of grid nodes required for accurate supersonic flow field computations. The code is fully vectorizable. Also, the code efficiently exploits multiprocessor architectures for parallel execution.

An area of particular interest in projectile aerodynamics is the nose tip.⁵ The findings of Reference 5 indicate that bluntness of 10% or less has no significant effect on the pitch plane aerodynamics of shell at supersonic velocities; however, bluntness of 10% was found to have a significant (25% at Mach 3) influence on the Magnus effect. Projectile nose tips are generally blunt with a flattened (meplate) front face. Typical nose bluntness (ratio of the meplate diameter to the maximum diameter of the shell) for artillery shell is 10-30%. Because of the bluntness, at supersonic speeds, the flow field contains a detached shock wave which results in a region of subsonic flow at the nose of the projectile. An experimental study on the influence of nose bluntness for a projectile was reported by Dolling and Gray.^{6,7} These data provide a challenging test case for computational aerodynamics since effects of the blunt nose are observed in the measured velocity profiles at downstream positions located between three and six calibers from the nose.

This report describes the evaluation of the capability of the new code to achieve accurate results and examines the degree of difficulty required to perform the computations. The computational performance achieved through the efficient utilization of the vector and parallel architecture on the Cray 2 and the Cray Y-MP supercomputers is defined.

II. GOVERNING EQUATIONS

The compressible, Reynolds-averaged, Navier-Stokes equations in a 3-D generalized coordinate system are written in the following strong conservation form. The dependent variables ρ, u, v, w and e are mass averaged, where e is specific total energy, T temperature, ρ mean density, p pressure, and t time.

$$\frac{\partial Q}{\partial t} + \frac{\partial (E - S)}{\partial \xi} + \frac{\partial (F - T)}{\partial \eta} + \frac{\partial (G - R)}{\partial \zeta} = 0 \quad (1)$$

The generalized coordinates are:

$$\xi = \xi(x, y, z) - \text{longitudinal coordinate}$$

$$\eta = \eta(x, y, z) - \text{near normal coordinate}$$

$$\zeta = \zeta(x, y, z) - \text{circumferential coordinate}$$

$$t = t - \text{time}.$$

The flux vectors are defined as:

$$Q = \frac{1}{J} \begin{bmatrix} \rho \\ \rho u \\ \rho v \\ \rho w \\ \rho e \end{bmatrix} \quad E = \frac{1}{J} \begin{bmatrix} \rho U \\ \rho u U + \xi_x p \\ \rho v U + \xi_y p \\ \rho w U + \xi_z p \\ (\rho e + p)U \end{bmatrix} \quad F = \frac{1}{J} \begin{bmatrix} \rho V \\ \rho u V + \eta_x p \\ \rho v V + \eta_y p \\ \rho w V + \eta_z p \\ (\rho e + p)V \end{bmatrix}$$

$$G = \frac{1}{J} \begin{bmatrix} \rho W \\ \rho u W + \zeta_x p \\ \rho v W + \zeta_y p \\ \rho w W + \zeta_z p \\ (\rho e + p)W \end{bmatrix} \quad S = \frac{1}{J} \begin{bmatrix} 0 \\ \xi_x \tau_{xx} + \xi_y \tau_{xy} + \xi_z \tau_{xz} \\ \xi_x \tau_{yx} + \xi_y \tau_{yy} + \xi_z \tau_{yz} \\ \xi_x \tau_{zx} + \xi_y \tau_{zy} + \xi_z \tau_{zz} \\ \xi_x \beta_x + \xi_y \beta_y + \xi_z \beta_z \end{bmatrix}$$

$$T = \frac{1}{J} \begin{bmatrix} 0 \\ \eta_x \tau_{xx} + \eta_y \tau_{xy} + \eta_z \tau_{xz} \\ \eta_x \tau_{yx} + \eta_y \tau_{yy} + \eta_z \tau_{yz} \\ \eta_x \tau_{zx} + \eta_y \tau_{zy} + \eta_z \tau_{zz} \\ \eta_x \beta_x + \eta_y \beta_y + \eta_z \beta_z \end{bmatrix} \quad R = \frac{1}{J} \begin{bmatrix} 0 \\ \zeta_x \tau_{xx} + \zeta_y \tau_{xy} + \zeta_z \tau_{xz} \\ \zeta_x \tau_{yx} + \zeta_y \tau_{yy} + \zeta_z \tau_{yz} \\ \zeta_x \tau_{zx} + \zeta_y \tau_{zy} + \zeta_z \tau_{zz} \\ \zeta_x \beta_x + \zeta_y \beta_y + \zeta_z \beta_z \end{bmatrix},$$

where

$$\tau_{xx} = -\frac{2}{3}(\mu + \varepsilon)(u_x + v_y + w_z) + 2(\mu + \varepsilon)u_x$$

$$\tau_{xy} = \tau_{yx} = (\mu + \varepsilon)(u_y + v_x)$$

$$\tau_{xz} = \tau_{zx} = (\mu + \varepsilon)(u_z + w_x)$$

$$\tau_{yy} = -\frac{2}{3}(\mu + \varepsilon)(u_x + v_y + w_z) + 2(\mu + \varepsilon)v_y$$

$$\tau_{yz} = \tau_{zy} = (\mu + \varepsilon)(v_z + w_y)$$

$$\tau_{zz} = -\frac{2}{3}(\mu + \varepsilon)(u_x + v_y + w_z) + 2(\mu + \varepsilon)w_z$$

$$\beta_x = C_P \left(\frac{\mu}{P_r} + \frac{\varepsilon}{P_{r_t}} \right) \frac{\partial T}{\partial x} + u\tau_{xx} + v\tau_{xy} + w\tau_{xz}$$

$$\beta_y = C_P \left(\frac{\mu}{P_r} + \frac{\varepsilon}{P_{r_t}} \right) \frac{\partial T}{\partial y} + u\tau_{yx} + v\tau_{yy} + w\tau_{yz}$$

$$\beta_z = C_P \left(\frac{\mu}{P_r} + \frac{\varepsilon}{P_{r_t}} \right) \frac{\partial T}{\partial z} + u\tau_{zx} + v\tau_{zy} + w\tau_{zz}$$

The molecular viscosity is μ and the turbulent viscosity is ε . The Jacobian of the generalized coordinates is:

$$J^{-1} = x_\xi y_\eta z_\zeta + x_\eta y_\zeta z_\xi + x_\zeta y_\xi z_\eta - x_\xi y_\zeta z_\eta - x_\eta y_\xi z_\zeta - x_\zeta y_\eta z_\xi.$$

The velocities in the ξ , η and ζ coordinates are:

$$U = \xi_x u + \xi_y v + \xi_z w$$

$$V = \eta_x u + \eta_y v + \eta_z w \quad (2)$$

$$W = \zeta_x u + \zeta_y v + \zeta_z w$$

which represent the contravariant velocity components.

The air was assumed to be a perfect gas, satisfying the equation of state

$$p = \rho RT \quad (3)$$

where R is the gas constant ($1716 \text{ ft}^2/\text{sec}^2 - {}^\circ\text{R}$ for air). For the dependence of laminar viscosity on the temperature, Sutherland's law was used:

$$\mu = 2.270 \frac{T^{3/2}}{T + 198.6} \times 10^{-8} \frac{\text{lb} - \text{sec}}{\text{ft}^2}. \quad (4)$$

The laminar and turbulent Prandtl numbers P_r and $P_{r,t}$, were assumed constant with values of 0.72 and 0.9, respectively. The ratio of specific heats was also assumed constant and equal to 1.4. The specific heat capacities at constant volume and constant pressure are C_v and C_p , respectively.

$$(C_v = 4290 \text{ ft}^2/\text{sec}^2 - {}^\circ\text{R} \text{ and } C_p = 6006 \text{ ft}^2/\text{sec}^2 - {}^\circ\text{R} \text{ for air}).$$

The total energy per unit mass, e , is given by

$$e = C_v T + 0.5(u^2 + v^2 + w^2). \quad (5)$$

The local pressure is determined using the following relation

$$p = \rho(\gamma - 1) [e - 0.5(u^2 + v^2 + w^2)]. \quad (6)$$

III. NUMERICAL METHOD

1. COMPUTATIONAL ALGORITHM

MacCormack's⁴ explicit and unsplit method is utilized for numerical integration of the governing Equations (1) in time from an assumed initial condition until a steady solution is obtained. The finite-difference method for the one-dimensional equation:

$$\frac{\partial Q}{\partial t} + \frac{\partial E}{\partial \xi} = 0 \quad (7)$$

is given by the following predictor - corrector steps:

$$Q_{i,j}^{\overline{n+1}} = Q_{i,j}^n - \frac{\Delta t}{\Delta \xi} (E_{i,j}^n - E_{i-1,j}^n) \quad (8)$$

$$Q_{i,j}^{n+1} = \frac{1}{2} \left[Q_{i,j}^n + \overline{Q_{i,j}^{n+1}} - \frac{\Delta t}{\Delta \xi} \left(\overline{E_{i+1,j}^{n+1}} - \overline{E_{i,j}^{n+1}} \right) \right] \quad (9)$$

where $\overline{E_{i,j}^{n+1}}$ implies that the terms are evaluated using $\overline{Q_{i,j}^{n+1}}$ and so forth. After completion of the above described two steps, first derivatives of the governing equations are approximated by second-order accurate central differences.

The reason for using the unsplit method over the time-split method is to save the number of accessions of the memory. In other words, for advancing one time-step, the unsplit method requires considerably fewer accessions to the memory than the time-split method. For the explicit method the time-step size must not exceed the maximum allowed by the CFL condition. An approximate linearized stability analysis for the inviscid equations yields the following:

$$\Delta t = \left[\frac{|U|}{\Delta \xi} + \frac{|V|}{\Delta \eta} + \frac{|W|}{\Delta \zeta} + c \left\{ \left(\frac{\xi_x}{\Delta \xi} + \frac{\eta_x}{\Delta \eta} + \frac{\zeta_x}{\Delta \zeta} \right)^2 + \left(\frac{\xi_y}{\Delta \xi} + \frac{\eta_y}{\Delta \eta} + \frac{\zeta_y}{\Delta \zeta} \right)^2 + \left(\frac{\xi_z}{\Delta \xi} + \frac{\eta_z}{\Delta \eta} + \frac{\zeta_z}{\Delta \zeta} \right)^2 \right\}^{\frac{1}{2}} \right]^{-1} \quad (10)$$

where c is the speed of sound. Since the terms involving molecular and eddy viscosity stabilize the solution, the time-step size computed using the inviscid analysis was found stable for both inviscid and viscous applications. Equation (10) was multiplied by a factor (denoted by CFL) that is slightly less than one.

For a truly time dependent solution, Δt obtained from Equation (10) must be the minimum value of the Δt for all field cells. Because of the non-uniformity of the grid spacing for the viscous flow calculations, the values of Δt can vary substantially within the field. Hence, the time dependent solution can converge very slowly if the convergence is constrained by the most restrictive condition within the flow field. However, when the steady state solution is of interest, a substantial improvement in the convergence rate can be obtained by using locally variable time steps. In other words, instead of using a minimum Δt of all field cells, each cell uses its local maximum allowable Δt .

2. NUMERICAL DAMPING

Flows containing strong shock waves cause numerical oscillations. In order to control these oscillations, two artificial dissipation terms were incorporated into the present numerical procedure. The resulting artificial dissipation term is a blending of second and fourth order differences. That is

$$D = (D_\xi^2 + D_\eta^2 + D_\zeta^2 - D_\xi^4 - D_\eta^4 - D_\zeta^4). \quad (11)$$

The second and fourth order differences for the dissipation are obtained using the following equations.

$$D_\xi^2 = \frac{\partial}{\partial \xi} [\lambda_\xi \nu] \frac{\partial Q}{\partial \xi} \quad (12)$$

$$D_\xi^4 = \frac{\partial}{\partial \xi} \left[\frac{\lambda_\xi}{(1 + \nu)} \right] \frac{\partial^3 Q}{\partial \xi^3} \quad (13)$$

where

$$\lambda_\xi = |U| + (\xi_x^2 + \xi_y^2 + \xi_z^2)^{\frac{1}{2}} c$$

$$\nu = \left(\frac{\Delta \xi^2}{4p} \right) \left(\frac{\partial^2 p}{\partial \xi^2} \right)$$

Note that Equation (12) is the damping suggested by MacCormack,⁴ which is only of significant magnitude in regions of pressure oscillations. This local effect prevents unrealistic oscillations in the neighborhood of shockwaves.

It is well known that central-difference schemes experience odd and even point decoupling for both linear and non-linear problems. These high frequency modes must be damped to enhance the convergence rate. The new terms, introduced by Equation (13) into the MacCormack algorithm, provide high frequency damping. The improvement in the convergence rate that can be obtained for a class of problems will be reported in a separate follow-up report.

The artificial dissipation terms were conveniently handled by adding them to appropriate flux vectors E , F and G of Equation (1).

3. ZONAL GRIDDING

The problem of computing the external flow field over a blunt nosed body is complex because of the presence of sharp corners. A conventional wrap-around grid requires rounding of these sharp corners and can result in rapid variation of the metric terms. However, this complex geometry can be efficiently gridded using the zonal grid approach. The complex nose geometry is broken into two zones of simple geometric shape. In each zone an algebraic grid generation technique is used with grid clustering near the surface.

A simple zone coupling technique has been used in the present work. In this technique, zonal grids share one grid cell boundary with geometric continuity of at least one grid cell

for overlapped zones. The coupling of zones is obtained by using one grid-cell overlap. This zonal-coupling is simple and transparent to shockwaves and separated boundary layers. The transparency of zonal-coupling is important because the initial conditions are very far from the steady state and, during the transient phase, shocks may travel through the overlapped boundaries. As shown in Figure 1, the zones coincide on a row of overlapped cells. The right-hand side boundary of zone A is contained within zone B and the left-hand side boundary of zone B is contained within zone A. Since overlapped cells are of the same shape in both zones, this approach requires transfer of information from the field of zone A to the boundary of zone B and vice-versa. This technique does not introduce any zonal boundary condition. In other words, the continuity in the solution across zones was obtained by simply exchanging data.

Each multi-zone solution was obtained by taking one time step in each zone and then exchanging boundary information between zones. This zone-coupling technique has worked well for both two-dimensional and three-dimensional applications.

4. BOUNDARY CONDITIONS AND TURBULENCE MODEL

The free-stream boundary conditions are held at the appropriate freestream values for the duration of the solution procedure. At the downstream boundary, the conventional zero gradient boundary condition is applied. The no slip boundary condition for viscous flow is enforced by setting the contravariant velocities to zero on the body surface. At the outer boundary, a no-reflection boundary condition is applied (Appendix A). This feature of the code enables solutions for supersonic flow to be achieved using a minimum of flow field grid nodes since the outer flow field can be significantly truncated. This feature is especially important for long length/diameter bodies.

For nonspinning projectiles at an angle of attack, symmetry exists about the projectile axis; therefore, the computation is performed only over the half body. Thus, symmetry boundary conditions are imposed at both ends in the circumferential direction. The pressure on the body surface is obtained by applying a normal pressure boundary condition using the momentum equations. For the body at $\eta = \text{const.}$, the normal pressure boundary condition is:

$$\begin{aligned} (\eta_x^2 + \eta_y^2 + \eta_z^2) p_\eta = - \{ (\zeta_x \eta_x + \zeta_y \eta_y + \zeta_z \eta_z) p_\zeta + (\xi_x \eta_x + \xi_y \eta_y + \xi_z \eta_z) p_\xi \\ + \rho U (\eta_x u_\xi + \eta_z w_\xi + \eta_y v_\xi) + \rho W (\eta_x u_\zeta + \eta_z w_\zeta + \eta_y v_\zeta) \}. \end{aligned} \quad (14)$$

For viscous flow, $U = W = 0$ is used in the above equation.

The temperature on the body surface is computed using the adiabatic wall condition. The initial condition is prescribed using the freestream condition.

For the computation of turbulent flows, a turbulence model must be supplied. In the present calculations, a two-layer algebraic eddy viscosity model due to Baldwin and Lomax⁸ is used. Following shadowgraph observations, transition to turbulence from laminar to turbulent viscous flow has been initiated on the ogive at 0.5 calibers downstream of the nose

tip. The transition from laminar to fully turbulent viscous effects was imposed gradually through an axial distance of 0.1 caliber.

IV. MODEL GEOMETRY AND EXPERIMENT

One means of validating a computer code for a particular class of problem is through comparison with available experimental data. The model used for the experimental and computational study presented here is an idealization of a realistic projectile nose geometry. A sketch of the model is shown in Figure 2. The model consists of a flat-faced nose, a three-caliber ogive, and a six-caliber cylindrical section. The experimental data^{6,7} used for comparison in this report were obtained in the Princeton University supersonic, high Reynolds number, blow-down tunnel. At the test section the value of M_∞ was 2.95. The supply header conditions were $P_0 = 14400 \text{ lbf/ft}^2$, $T_t = 468^\circ\text{R}$, giving a nominal test section $Re = 1.9 \times 10^7$ per foot. The pressure and velocity profile data were obtained at 0° and 2.9° angle of attack at the wind and lee-sides.

V. COMPUTATIONAL RESULTS

All computations were performed on the CRAY-2 supercomputer at BRL. As mentioned earlier, the solution technique involves solving the 3-D, time dependent, full Navier-Stokes equations. The procedure is started by assuming uniform free-stream conditions for all field points. A slow start of the boundary condition is implemented and the calculation marches in time until a steady state solution is obtained. A criterion for convergence rate is established by the magnitude of the variation of the root mean square of the residual of the continuity equation with iteration. Also, the surface pressure distribution is checked for time invariance. For this application, 2000-3000 iterations using the local, variable, time step technique were found to provide a converged solution.

A two zone grid for the present calculations was algebraically generated. Figure 3 shows the surface grid with the lee and wind-side planes. The grid size for zone 1 and zone 2 were $(30 \times 90 \times 39)$ and $(161 \times 50 \times 39)$, respectively. Thirty-nine circumferential planes were placed uniformly giving five degrees of spacing between adjacent planes. In the radial direction, grid points were clustered using a hyperbolic tangent function. The grid spacing in the radial direction at the body surface was 2.564×10^{-4} calibers. The outer boundary in the radial direction was placed at 0.5 caliber from the body surface. An expanded view of the grid in the nose region is shown in Figure 4.

The flow over the flat nose tip consists of an over-expansion around the sharp corner followed by a recompression. The recompression is strong enough to produce an oblique shock wave. The flow separates in the streamwise direction in the vicinity of the corner. Figure 5 is a wind tunnel shadowgraph at $\alpha = 0^\circ$. Computed Mach number contours for $\alpha = 0^\circ$ are shown in Figure 6. These compare well with qualitative features of the flow field shown in the shadowgraph. Note that the detached bow shock and the recompression shock immediately downstream of the leading edge corner were successfully captured in

the computations.

Figure 7 shows the computed and measured surface pressure distribution for $\alpha = 0^\circ$. The arc distance on the x axis is measured from the axis of symmetry point of the flat-faced nose tip. Good agreement between computation and experimental data is achieved, including the region of over-expansion. Figure 8 shows computed and measured velocity profiles at three different stations. Stations 1, 2 and 3 are located at $X/D = 2.86, 4.65$ and 5.93 from the flat nose tip, respectively. The agreement achieved between computation and experiment is considered to be highly encouraging but not fully satisfactory. The largest discrepancy between computation and experiment is about three percent of the free stream velocity.

Next, the $\alpha = 2.9^\circ$ case was considered. A shadowgraph for this flow condition is shown in Figure 9. As expected, the wind-side recompression shock moves upstream and increases in strength while the opposite occurs on the lee-side. The computed Mach contours for this case are shown in Figure 10. The experimentally observed shift in shock pattern is predicted. Also, the computed and experimental surface pressure distributions agree well (Figure 11) for both the wind and lee-sides.

Figure 12 shows computed and measured velocity profiles for the lee-side at stations 1, 2 and 3. Figure 13 shows comparisons between computed and measured velocity profiles for the wind-side. Agreement between computation and experiment is, again, considered to be highly encouraging but not fully satisfactory. The largest discrepancy was about seven percent of the free stream velocity on the wind-side and about five percent of the free stream velocity on the lee-side.

The results at the down-stream stations are strongly affected by the accuracy of the modeling in the vicinity of the bow shock which, for this flat nosed case, contained local flow separation at the leading edge corner of the ogive. A consistent feature of the disagreement between computational and experimental velocity profiles is in the lower portion of the viscous layer at all measurement stations. This could be the effect of a deficiency of the turbulence model which does not account for flow field history. The flow field history effect resulting from the extreme expansion around the flattened nose and local flow separation could be significant. Another possibility is that increased grid resolution is needed near the surface. These possibilities will be addressed in future studies. Another consideration to be kept in mind is that of probe-wall interference which limits the accuracy of pitot-probe measurements in the vicinity of a wall.

The single processor CPU time for a laminar solution on a grid consisting of 419250 grid points was about 10 sec/iteration. The CPU time for a solution including turbulent viscous effects was about 11 sec/iteration for a solution converging for 4000 time steps in which the turbulence quantities were recomputed every 10 time steps. Values for the smoothing parameters were determined by performing trial runs using the axisymmetric version of the code. The three-dimensional computations were found to proceed without any special user interaction by using the predetermined values of the smoothing parameters. Of particular significance for this test case is that the flattened nose tip did not impose flow field convergence problems.

VI. PARALLEL IMPLEMENTATION AND PERFORMANCE

The mapping of complex physical zones onto processors is an important issue for efficient implementation on parallel computers. The partitioning across processors for 3D zonal applications can be done in the coarse to medium granularity range on shared memory processors. In the coarse granularity approach, a zone or subregion of a zone would be mapped on each processor. In general, the approach chosen will be application dependent. When a number of zones and/or size of zones change from one application to another, a new mapping procedure may be required. Also, it will be difficult to evenly distribute work among the processors when zone sizes vary by considerable magnitude. This would result in inefficient load balancing among the processors. In other words, some processors will finish their work faster than others and will be idle.

In the medium granularity approach, all processors work on a single zone in parallel. This parallelization consists of decomposing a zone at DO-loop level. For a 3D zone, each processor can be assigned to work on a 2D plane. Since no artificial boundaries are introduced on shared memory machines, this approach generally results in better load balancing than the coarse granularity approach. On Cray multiprocessors, this can be implemented using microtasking directives such as DO GLOBAL. On Crays, an inner DO-loop of a 2D plane can be executed in vector mode. Also, this approach is a natural way to partition a 3D zone because it maintains the physical zone intact.

There are two related issues to be addressed for efficient implementation of a solution algorithm on shared memory multiprocessors: (1) synchronization overhead; and (2) convergence rate. The synchronization overhead arises when processors have data dependencies which cause them to be idle. This can happen when global information is required to continue the solution process. For the present algorithm, this situation arises when one uses a global minimum time step size for time dependent calculations. Generally, the convergence rate of a parallel algorithm is related to synchronization overhead. In order to keep synchronization overhead to a reasonable magnitude, many parallel algorithms utilize readily available information instead of the best possible information. An example of this is that Jacobi and multi-color iterative methods are preferred over the Gauss-Seidel iterative method for parallel implementation. In the present implementation substantial synchronization overhead can arise when using a global minimum time step size for time integration. However, when only steady state solutions are of interest, the convergence rate can be improved by using a local maximum time step size (Section III). Fortunately, the local time step size procedure is highly parallel. The use of a local time step size not only eliminates the synchronization overhead associated with time step calculations, but improves the rate of convergence of the solution algorithm.

The parallel implementation of each time step integration can be summarized as follows. For the explicit method (Section III) with local time step size, the integration algorithm reduces to the classical fork and join procedure of parallel implementations. We must have all information on the RHS of Equation (8) available before we can fork or start solving Equation (8) in parallel. We must finish solving Equation (8) for every interior grid point for all zones (join) before we can fork and start forming the flux vectors for the

RHS of Equation (9). The fork and join procedure is used not only for solving Equations (8 and 9), but also for computing flux vectors, damping terms, time step size and so forth. Thus, the overall solution algorithm is highly parallel.

To evaluate the performance of the algorithm for an application that requires substantial memory, the complex 3D flow for a flat-nosed projectile discussed previously has been considered. The cost-effectiveness or the efficiency of the parallel implementation is measured in terms of speed-up or wall-clock execution time. The speed-up is defined as the ratio of the single processor execution time of a given algorithm to that of multiprocessor execution time of the same algorithm. Figure 14 shows the speed-up of the parallel implementation on Cray-2. The speed-up of 3.8 was achieved for this application on four processors of the Cray-2. This translates into 98.5% parallel efficiency. Figure 15 shows the speed-up achieved on eight processors of the Cray Y-MP. The code achieved a speed-up of 6.8 on eight processors. Again, this indicates a parallel efficiency of 97% on the Cray Y-MP. The speed-up on the Cray-2 and Cray Y-MP supercomputers were obtained by explicitly incorporating microtasking directives, not by using an autotasking preprocessor. The maximum efficiency that could be achieved for this application may be higher than reported here due to the fact that several computations such as boundary conditions, zonal overlap exchange, etc., were not executed in parallel.

VII. CONCLUDING REMARKS

This report has described the development of a three dimensional, unsteady, zonal, Navier-Stokes code which has been structured to efficiently utilize the vector/parallel architecture of modern supercomputers. The code has been applied to predict the flow field around a blunt-nosed projectile at supersonic speeds. Computational predictions were compared to experimental data for surface pressure distributions and velocity profiles. The results achieved indicate that the zonal topology provides accurate and efficient computational performance for the flattened (meplate) nose shape.

Although theoretical analysis and computations for ideal problems can indicate some general trends, the achievement of efficiency for computational execution is best demonstrated for a realistic 3D application. This study has shown the potential to reduce wall-clock time by tasking idle processors. For many similar 3D zonal applications on present supercomputers this can result in substantially enhanced turn-around times.

Future development of this code will be to extend the capabilities to perform computations for highly complex configurations such as guided, non-axisymmetric and finned body shapes.

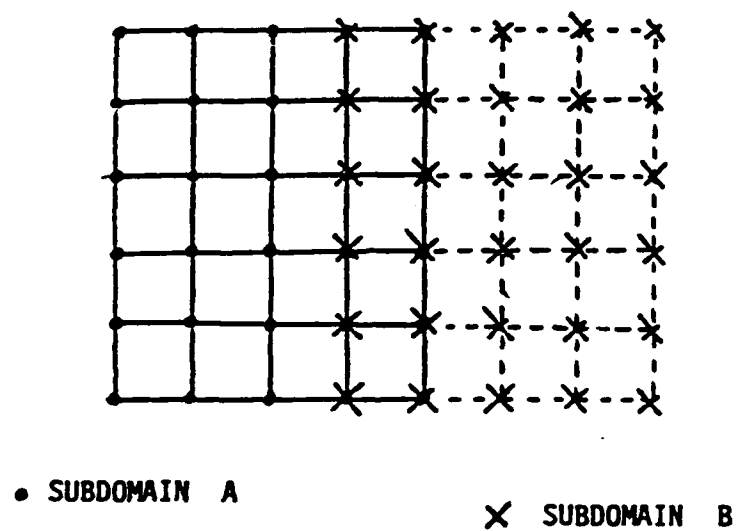


Figure 1. Schematic illustration of single grid-cell overlap.

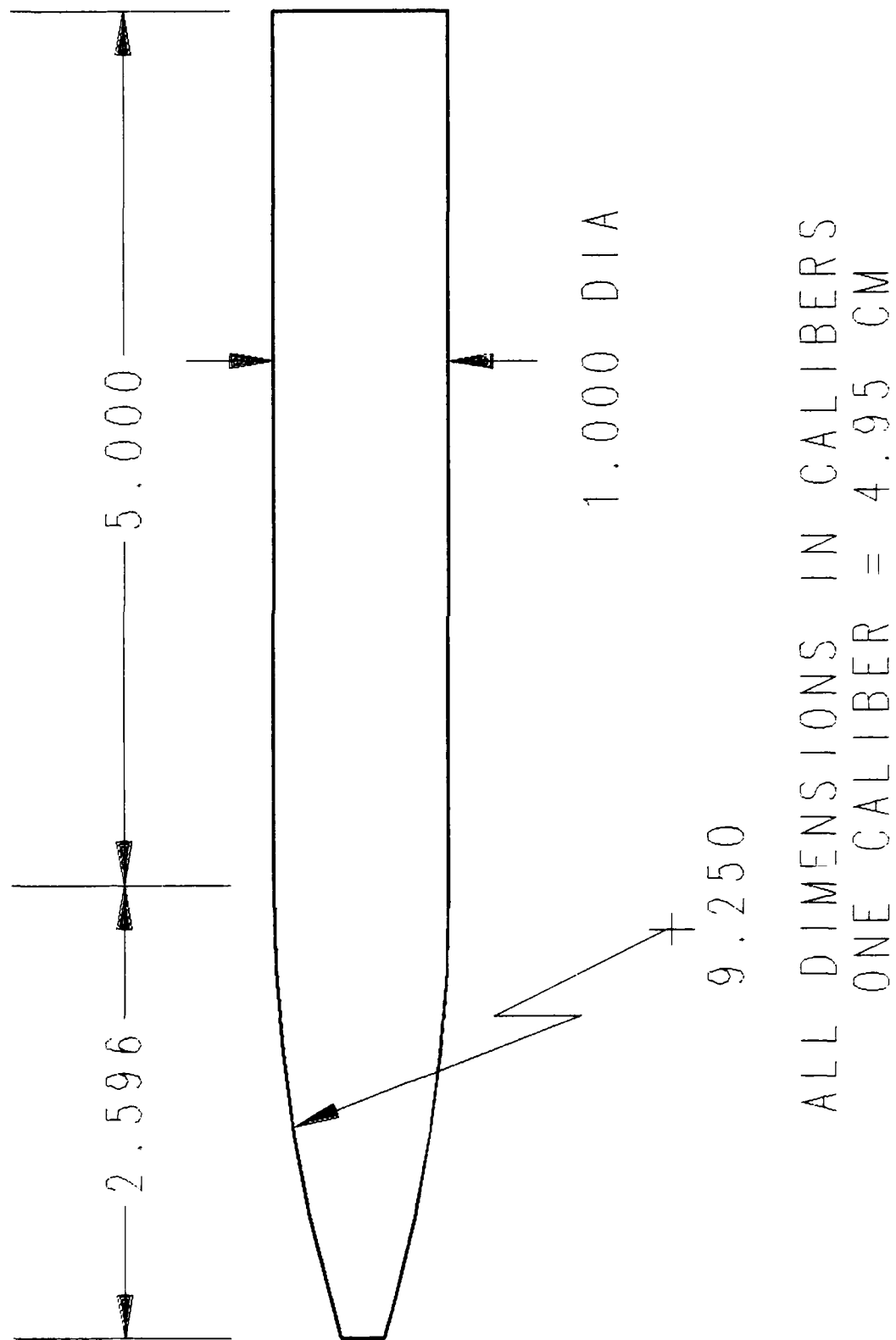


Figure 2. Schematic of the model.

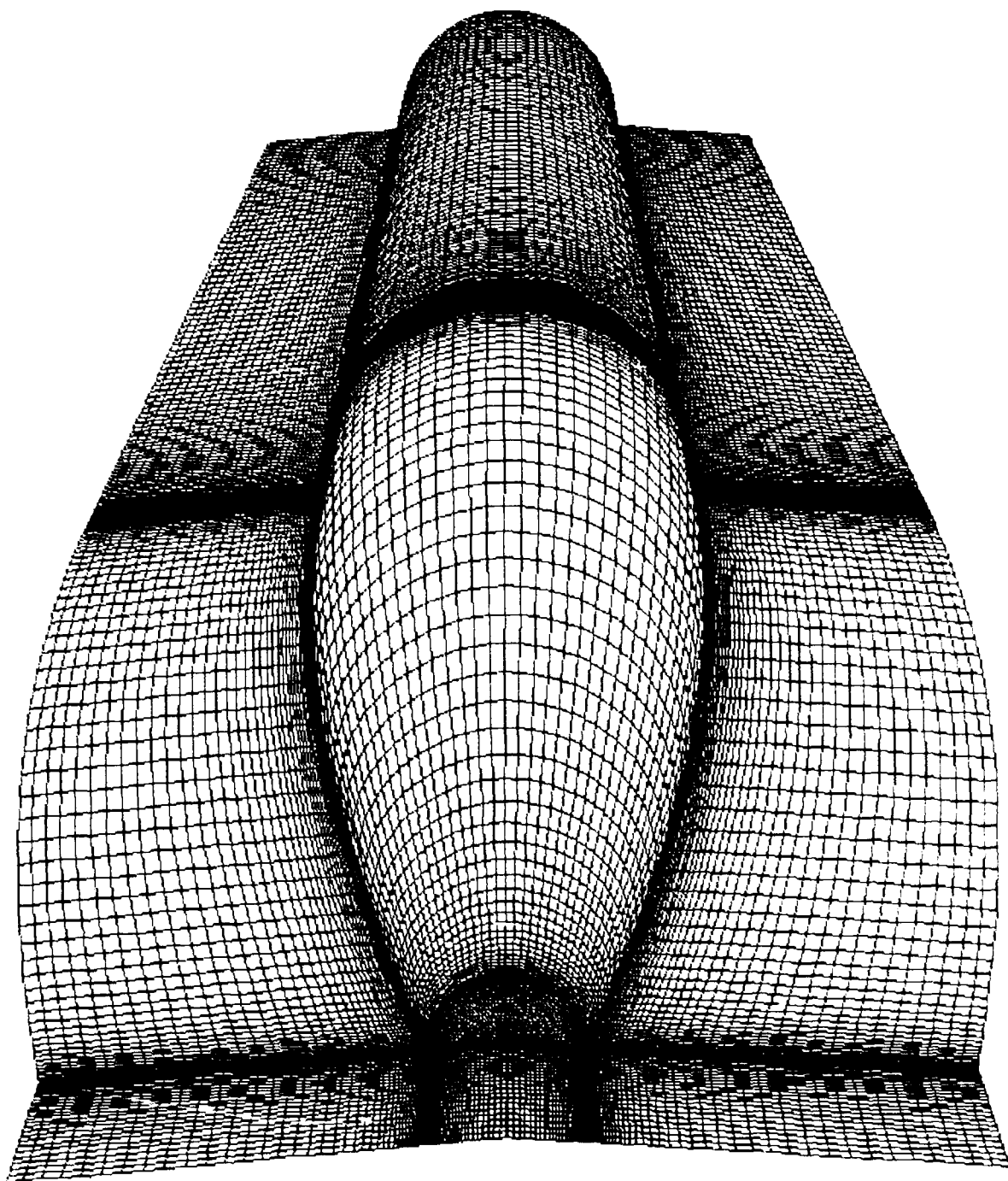


Figure 3. Body surface and pitch plane computational grid.

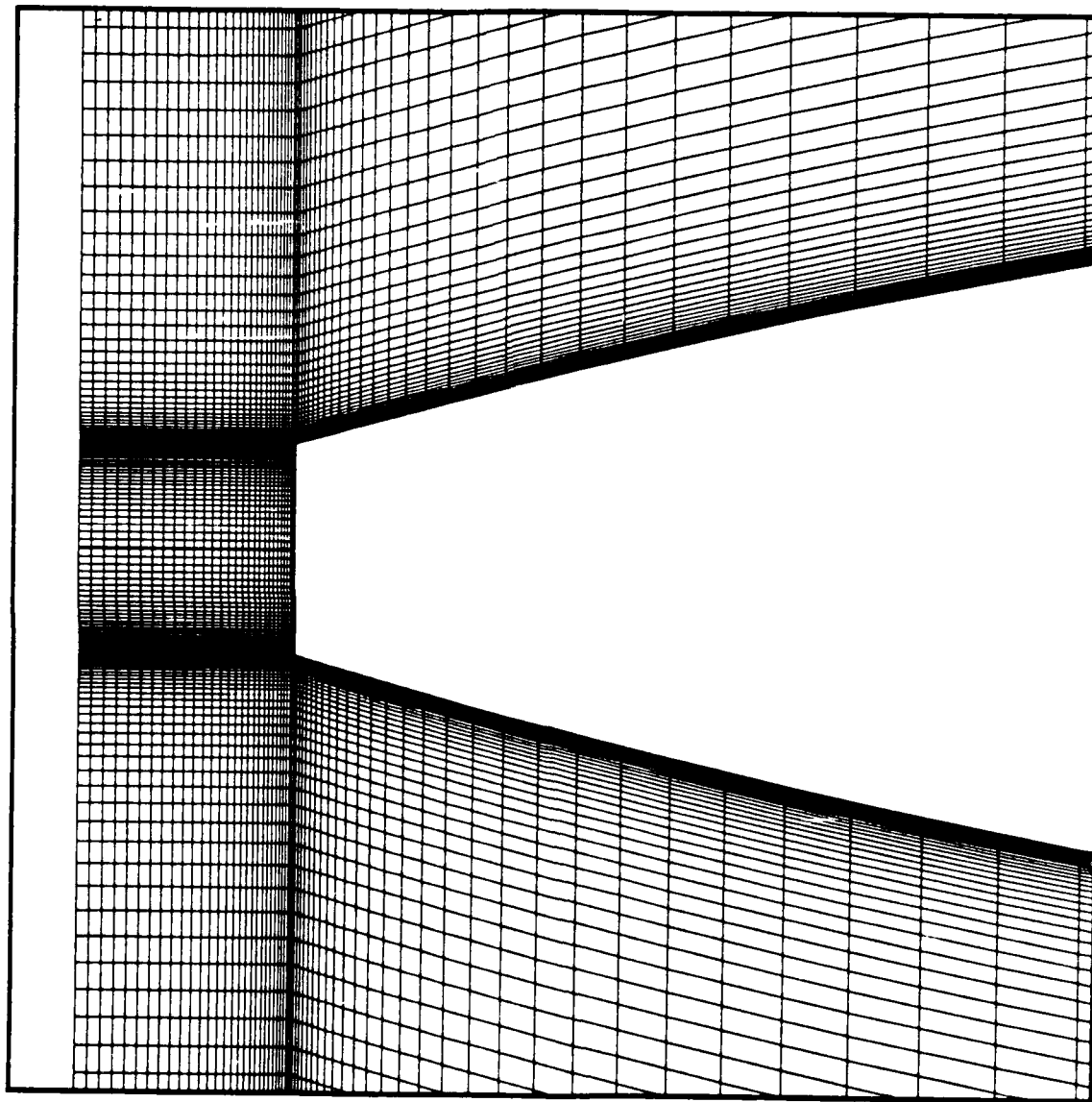


Figure 4. Pitch plane computational grid, nose region.

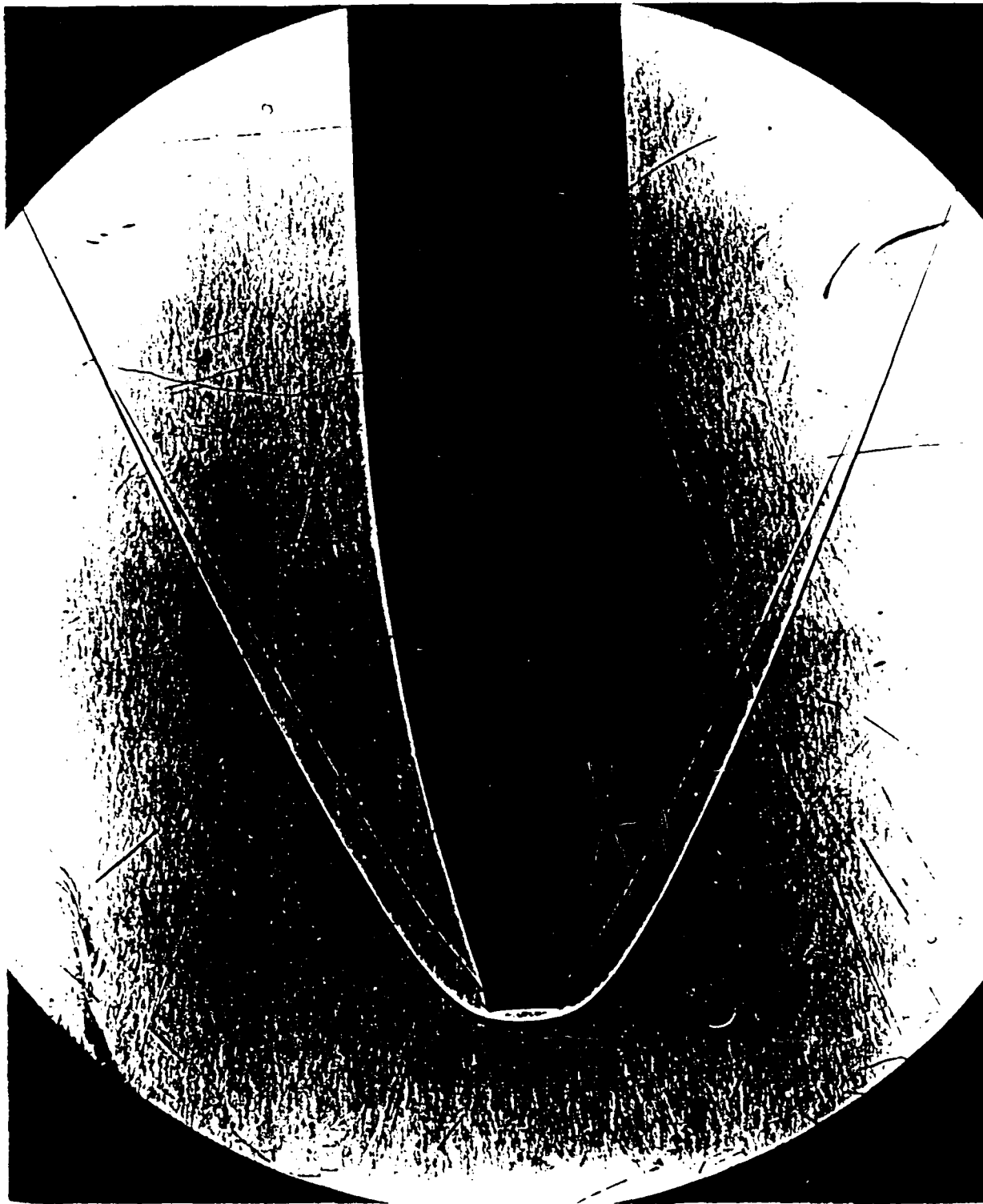


Figure 5. Wind tunnel spark shadowgraph of flow over blunt model, $M = 2.95$, $\alpha = 0.0^\circ$.

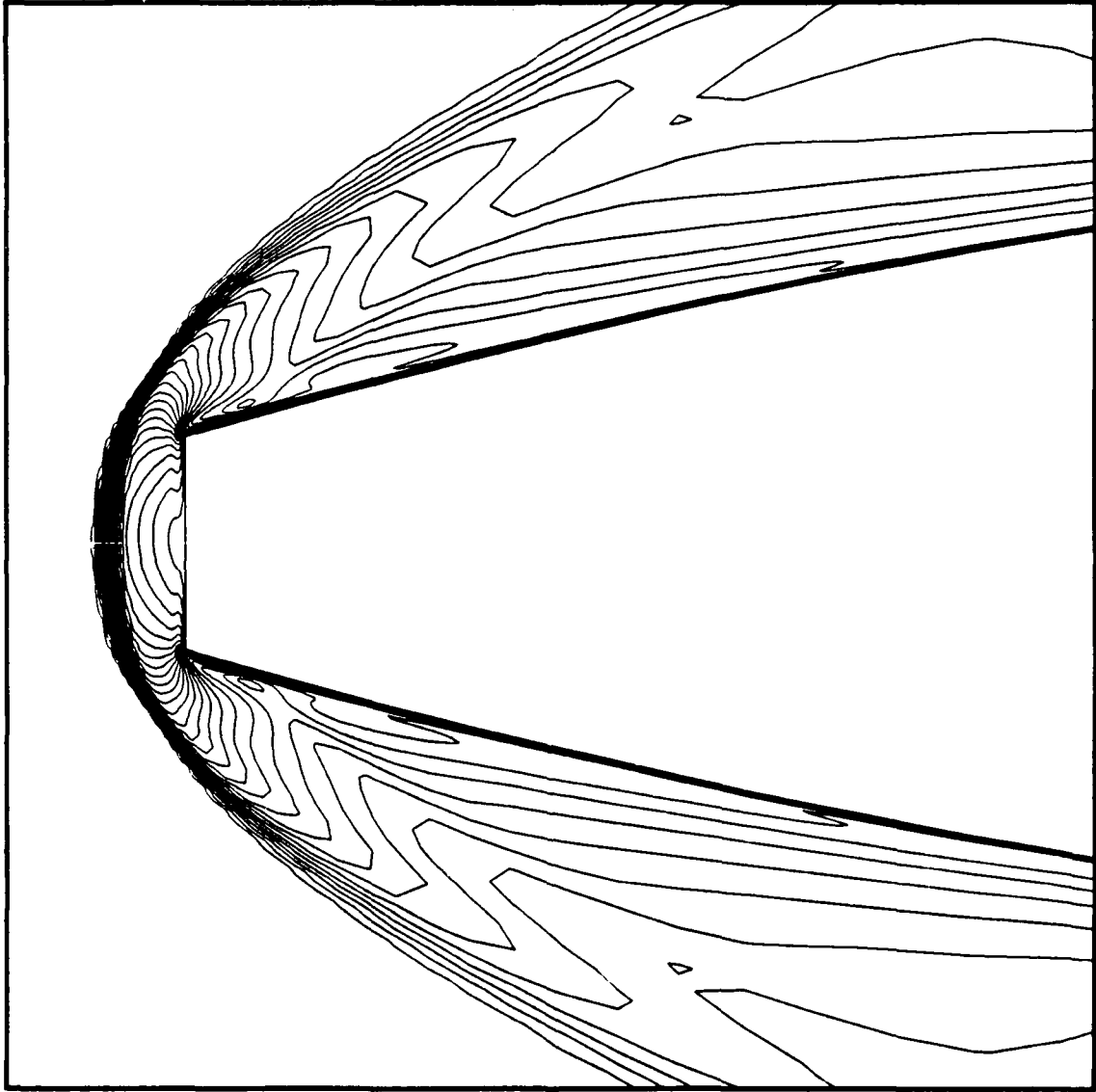


Figure 6. Computational results, Mach contour in nose region, $\alpha = 0.0^\circ$.

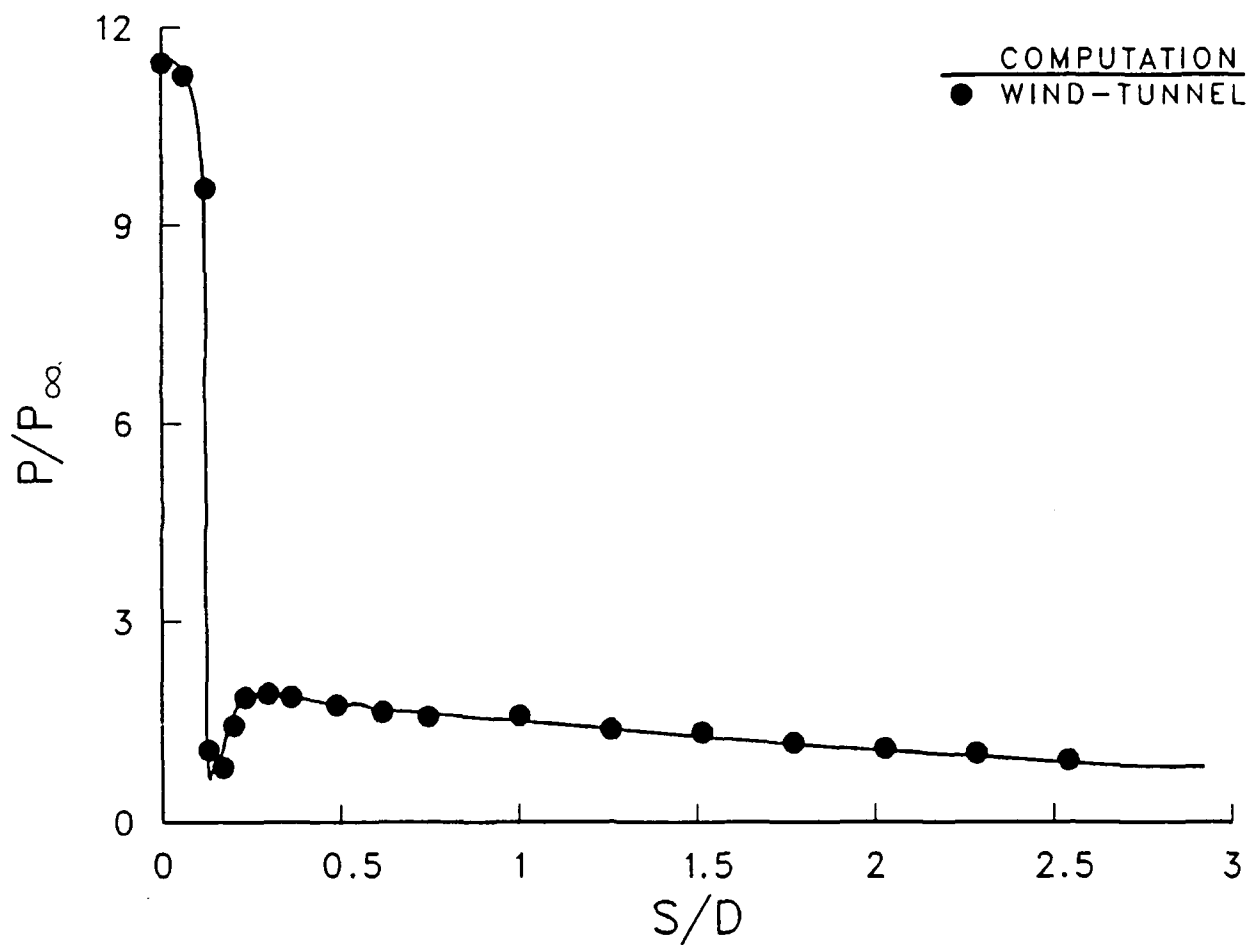


Figure 7. Surface pressure distribution, computation compared to experiment, $\alpha = 0.0^\circ$.

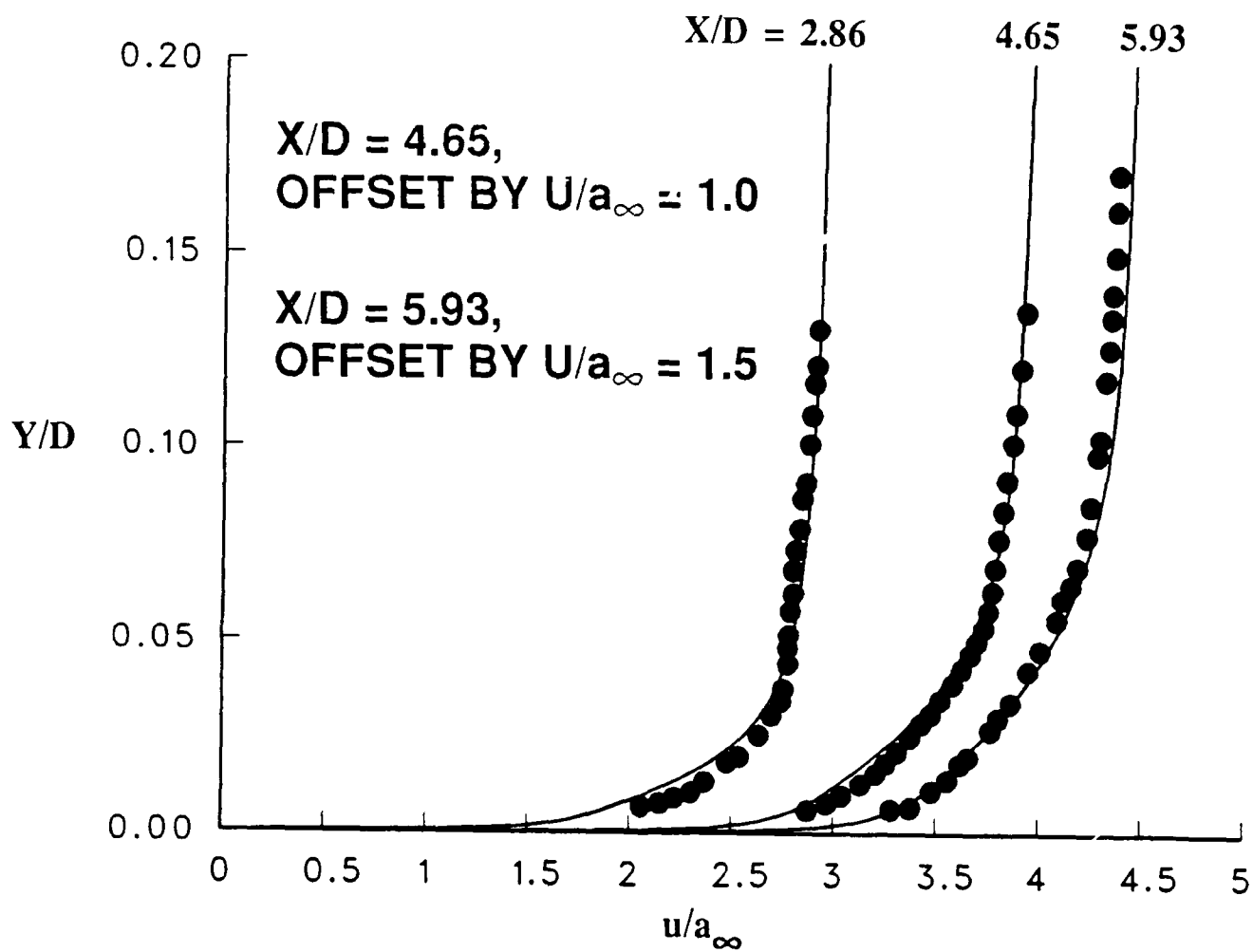


Figure 8. u -velocity profile, computation compared to experiment, $\alpha = 0.0^\circ$, $X/D = 2.86, 4.65$ and 5.93 .

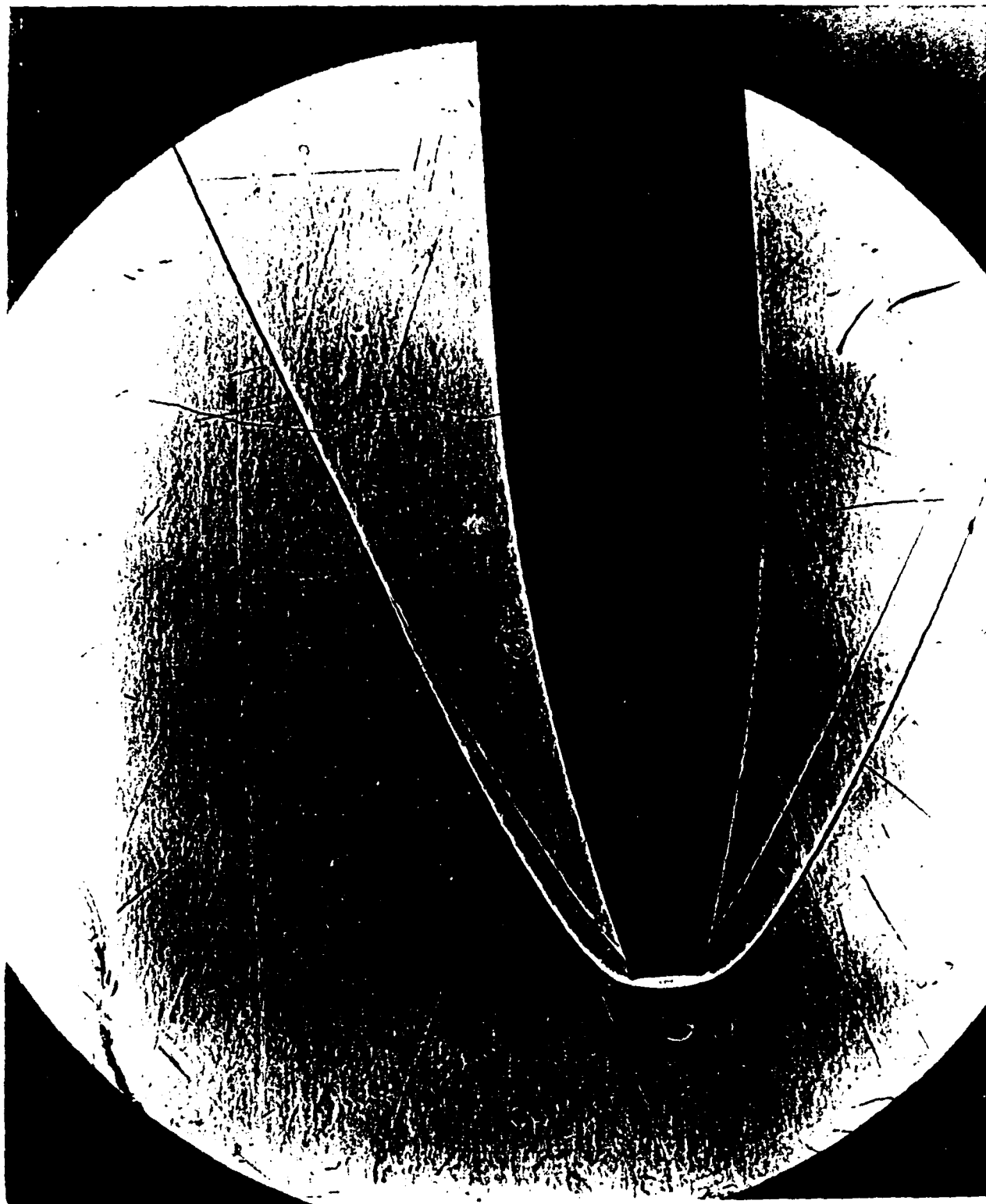


Figure 9. Wind tunnel spark shadowgraph of flow over blunt model, $M = 2.95$, $\alpha = 2.9^\circ$.

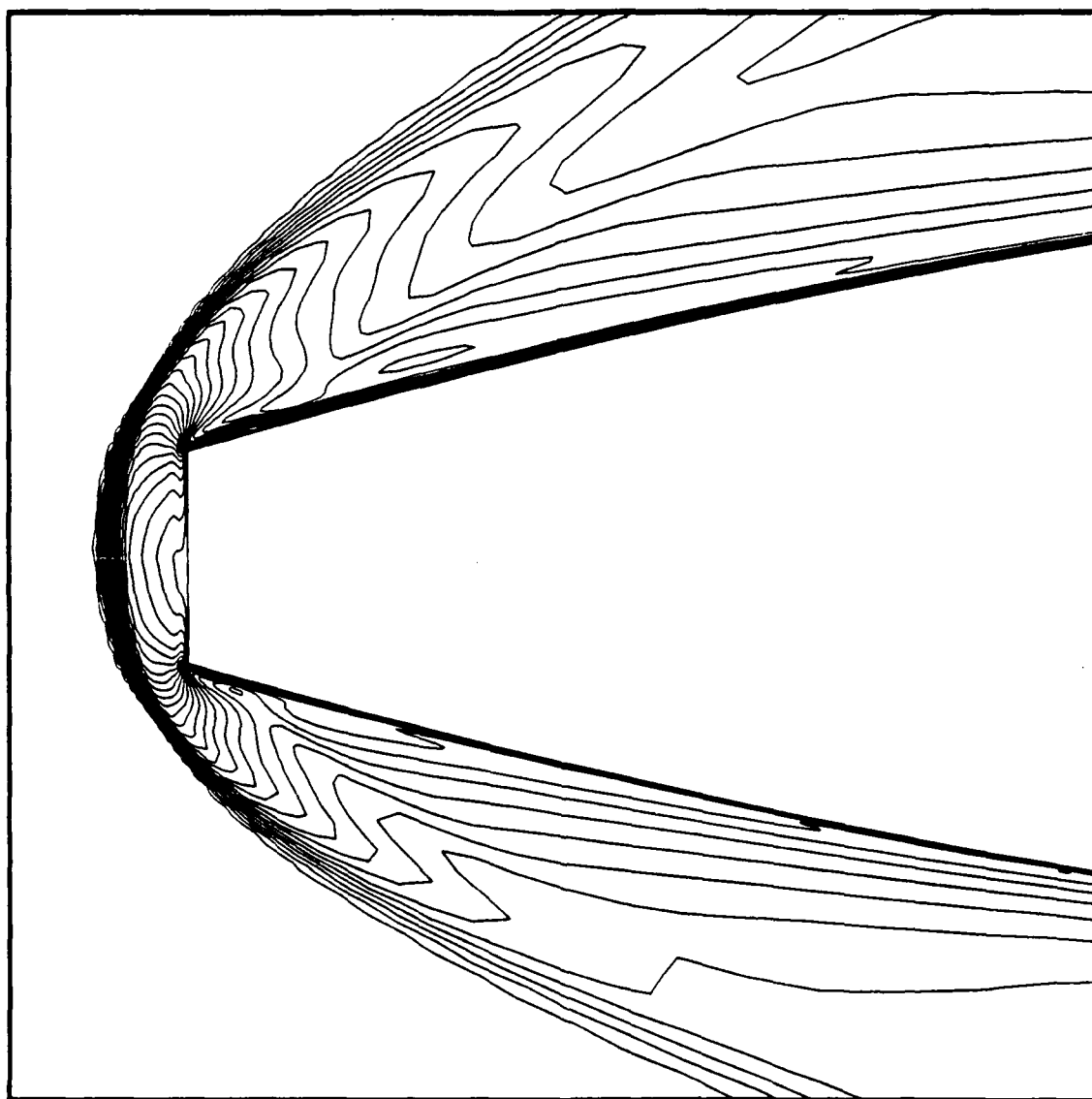


Figure 10. Computational results, Mach contour in nose region, $\alpha = 2.9^\circ$.

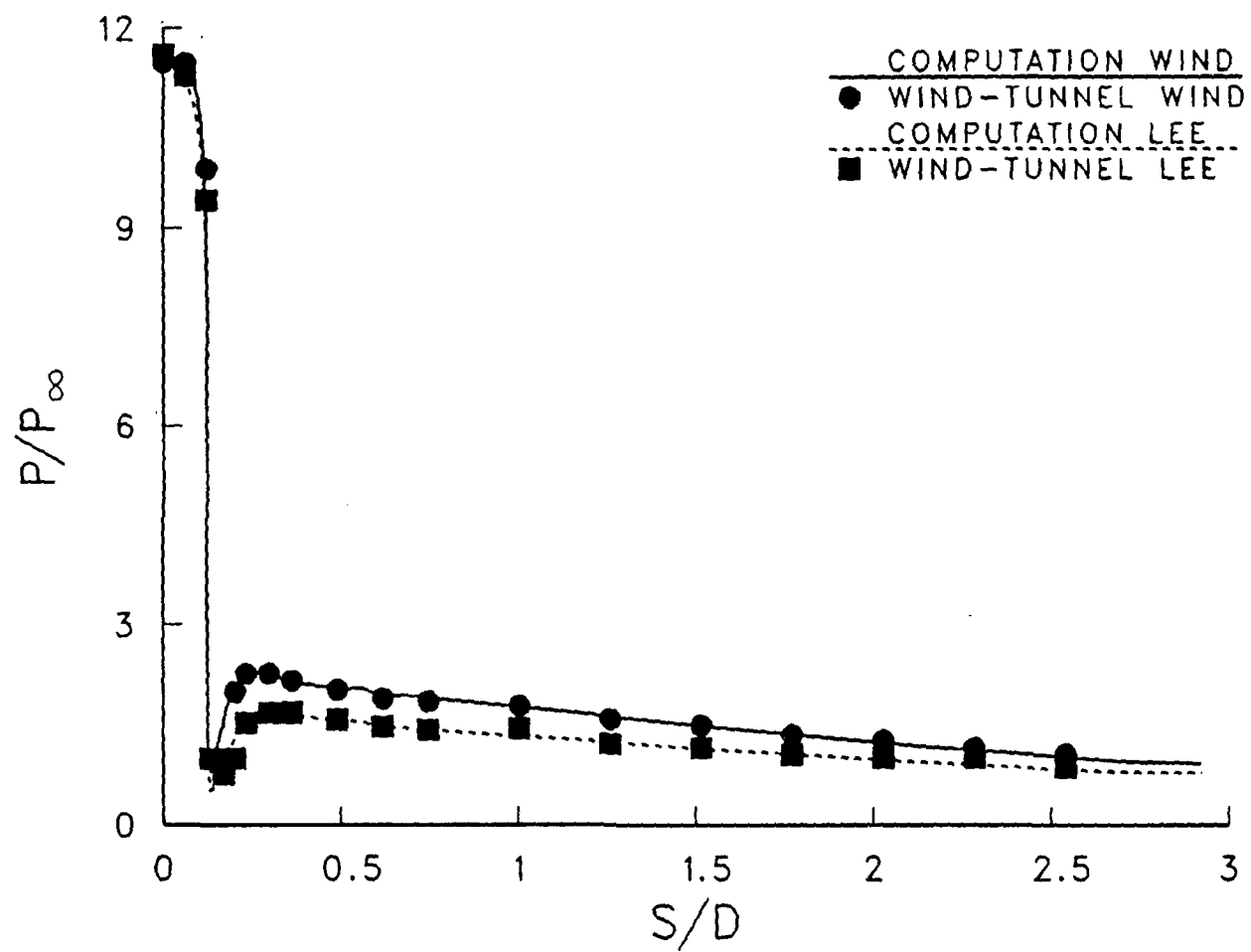


Figure 11. Surface pressure distribution, computation compared to experiment, $\alpha = 2.9^\circ$, wind and lee-side.

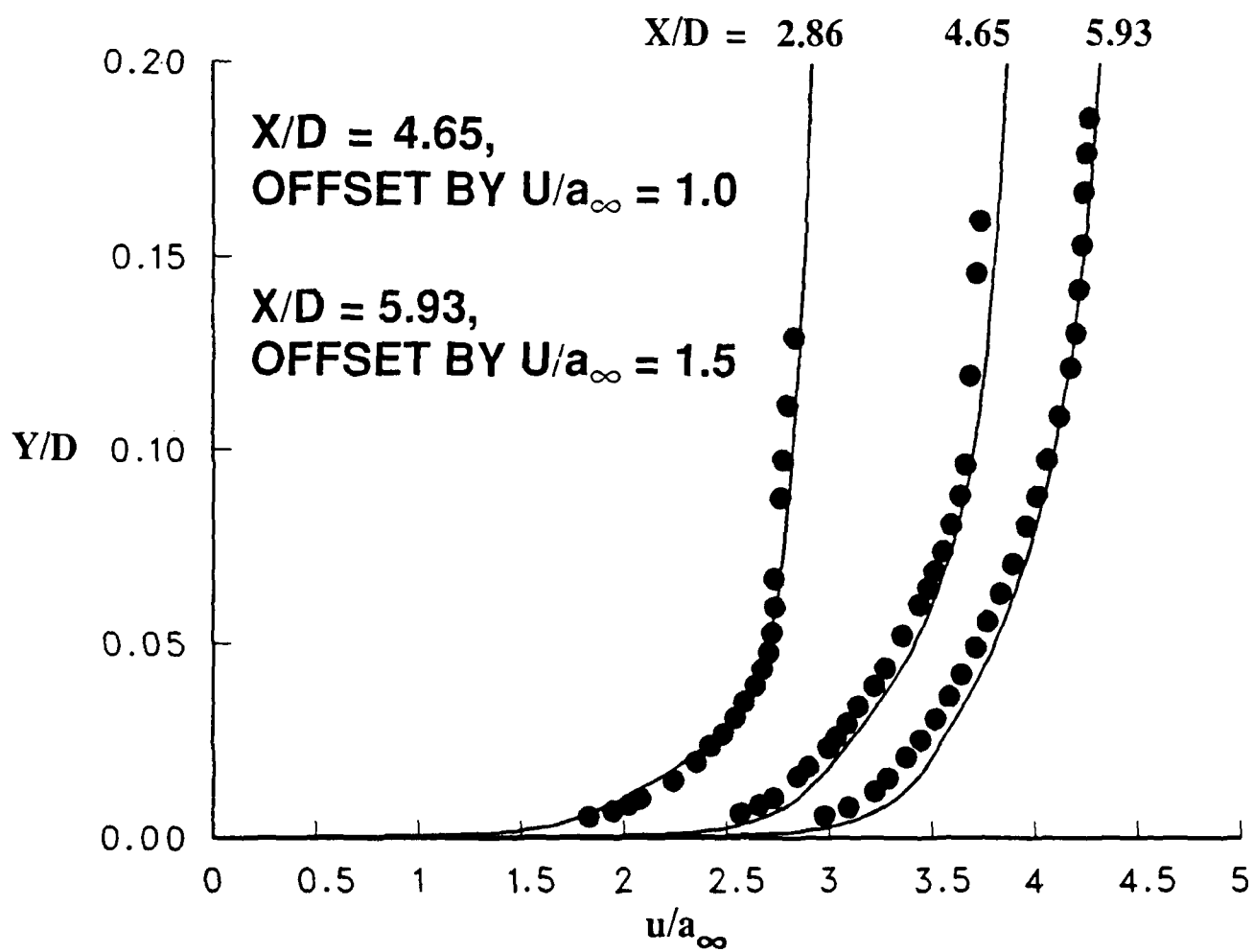


Figure 12. u -velocity profile, computation compared to experiment,
 $\alpha = 2.9^\circ$, $X/D = 2.86$, 4.65 and 5.93 , lee-side.

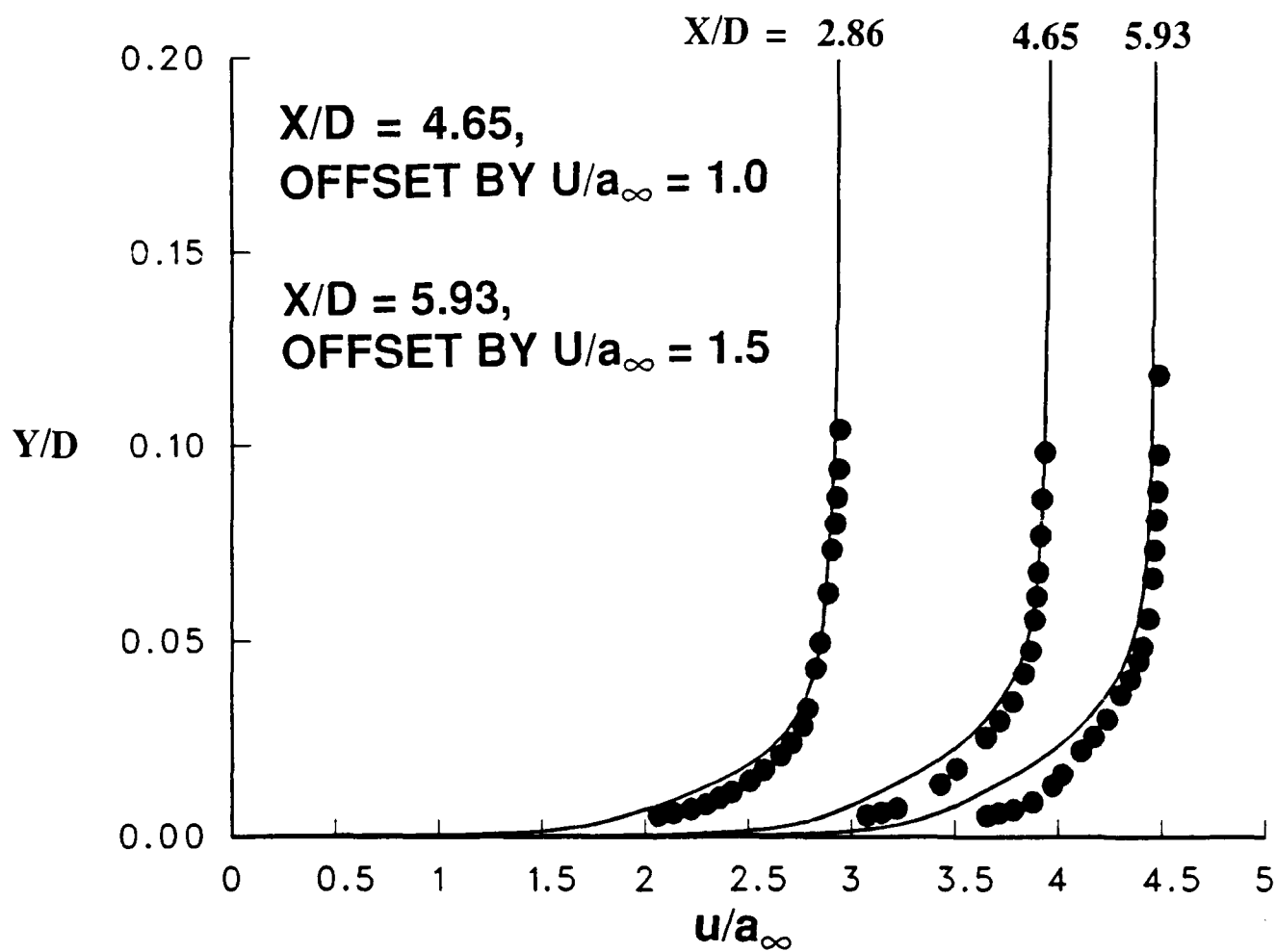


Figure 13. u-velocity profile, computation compared to experiment,
 $\alpha = 2.9^\circ$, $X/D = 2.86, 4.65$ and 5.93 , wind-side.

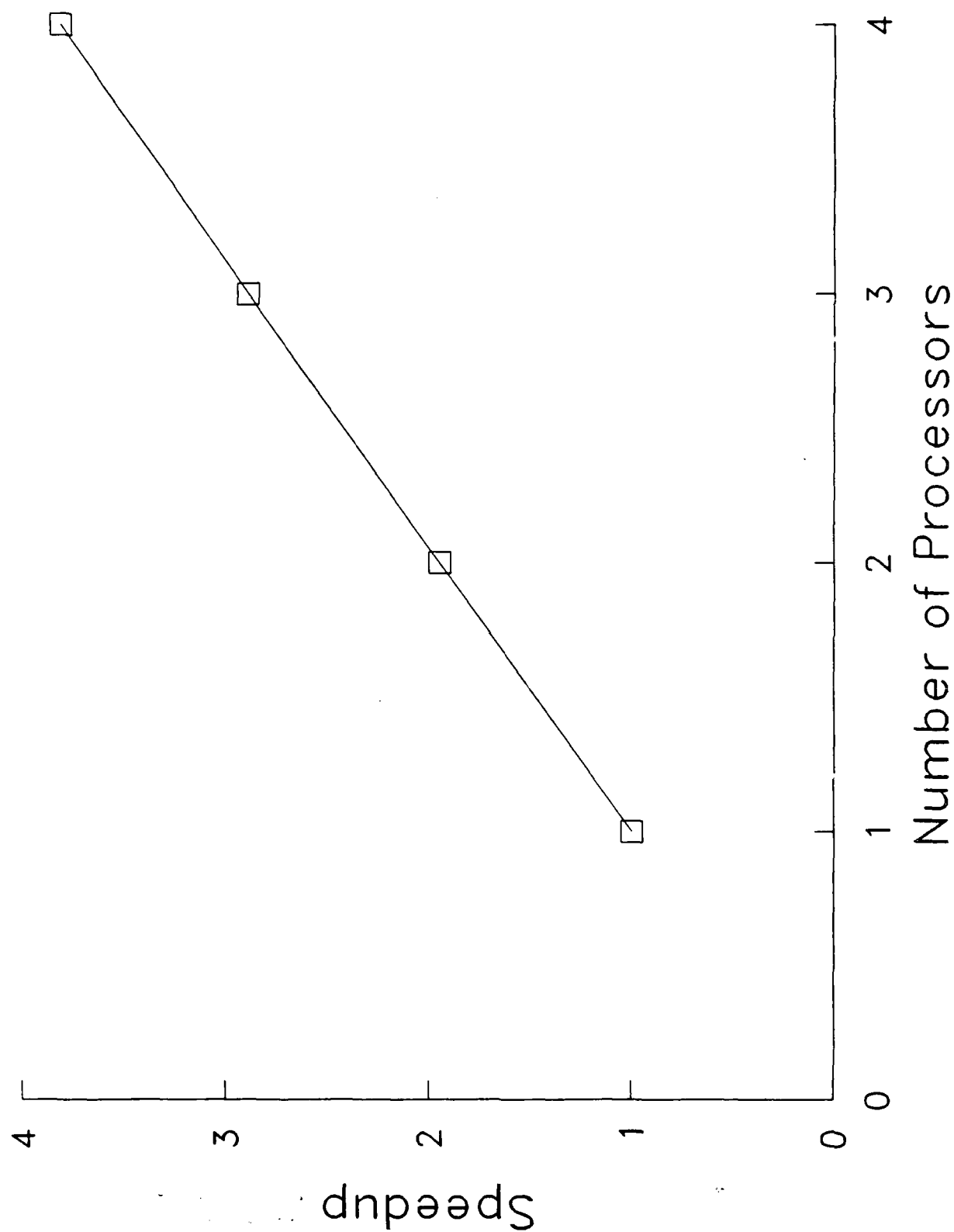


Figure 14. Speedup on Cray-2 - 3D microtasked code.

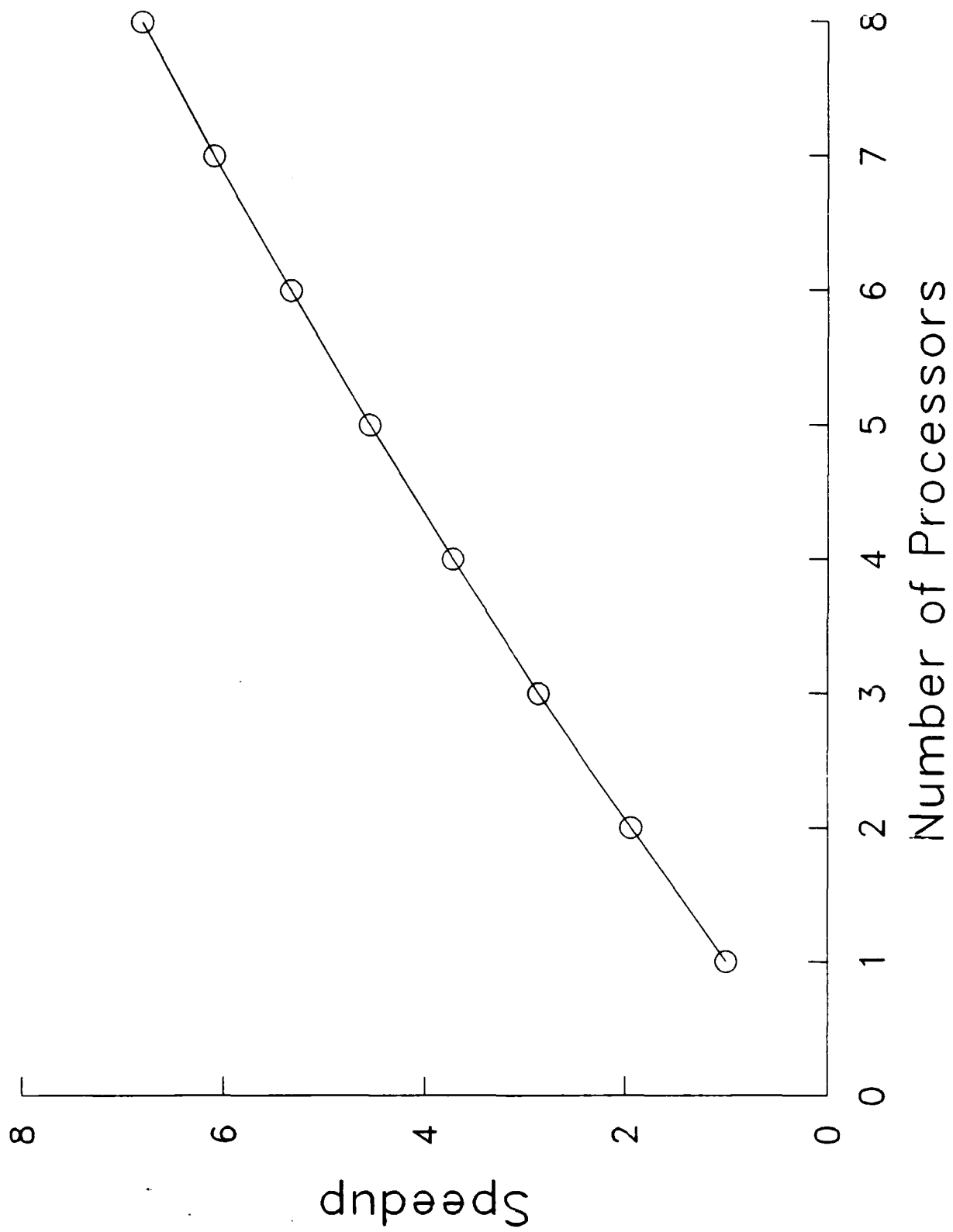


Figure 15. Speedup on Cray Y-MP - 3D zonal code.

References

1. Sturek, W.B., "Application of CFD to the Aerodynamics of Spinning Shell," AIAA Paper 84-0323, January 1984.
2. Nietubicz, C.J. and Sturek, W.B., "Navier-Stokes Code Verification for Projectile Configurations at Supersonic and Transonic Velocities," AIAA Paper No. 88-1995, AIAA 15th Aerodynamic Testing Conference, May 1988.
3. Patel, N.R., Sturek, W.B., and Hiromoto, R.E., "A Parallel Compressible Flow Algorithm for Multiprocessors," Applications of Parallel Processing in Fluid Mechanics, Fluids Engineering Division, Vol. 47, ASME, June 1987.
4. MacCormack, R.W., "The Effects of Viscosity in Hypervelocity Impact Cratering," AIAA Paper No. 69-354, 1969.
5. Sturek, W.B., Guidos, B., and Nietubicz, C.J., "Navier-Stokes Computational Study of the Magnus Effect on Shell with Small Bluntness at Supersonic Speeds," AIAA Paper No. 82-1341, AIAA 9th Atmospheric Flight Mechanics Conference, August 1982.
6. Doling, D.S. and Gray, W.K., "Experimental Study of Supersonic Turbulent Flow on a Blunted Axisymmetric Body," AIAA Journal, Vol. 24, No. 5, May 1986.
7. Dolling, D.S. and Gray, W.K., "Compilation of Wall Pressure and Turbulent Boundary Layer Data for Supersonic, High Reynolds Number Flow Over a Blunted Tangent Ogive Cylinder at Small Angles of Attack," Report No. 1585-MAE Princeton University, Mechanical and Aerospace Engineering Department, Princeton, New Jersey, September 1982.
8. Baldwin, B.S. and Lomax, H., "Thin Layer Approximation and Algebraic Model for Separated Flows," AIAA Paper No. 78-257, January 1978.

INTENTIONALLY LEFT BLANK.

APPENDIX A: NON-REFLECTING OUTER BOUNDARY CONDITION

This appendix describes the derivation of the non-reflection boundary condition employed along the top boundary. This boundary condition is consistent when the following conditions are met.

- (1) The local Mach number is greater than one at the boundary.
- (2) There is only one outwards running Mach line. This requirement is met if the local normal Mach number at the boundary is less than one.

Consider a nonorthogonal coordinate system as shown in Figure A1. Through point x, y one can draw the velocity vector and the Mach wave inclined at an angle μ with respect to the velocity vector. The velocity vector is at an angle ω measured with respect to Cartesian coordinate x . This can be indicated as:

$$\mu = \sin^{-1} \left(\frac{1}{M} \right)$$

and

$$\omega = \tan^{-1} \left(\frac{v}{u} \right)$$

which leads to a total included angle

$$\theta = \mu + \omega.$$

Let

$$f = f(\rho, u, v, T)^T.$$

The non-reflection condition requires that the flow variables remain constant along the left running Mach lines.

$$f_{i, JL} = f_{x, y}$$

which gives

$$f_{x, y} = f_{k-1, JL-1} + \frac{A}{B(f_{k, JL-1} - f_{k-1, JL-1})}$$

where

$$A = \left\{ (\tilde{x} - x_{k-1, JL-1})^2 + (\tilde{y} - y_{k-1, JL-1})^2 \right\}^{\frac{1}{2}}$$

$$B = (\Delta x^2 + \Delta y^2)^{\frac{1}{2}}$$

$$\Delta x = x_{k, JL-1} - x_{k-1, JL-1}$$

and

$$\Delta y = y_{k,JL-1} - y_{k-1,JL-1}$$

$$\Psi = \tan^{-1} \left(\frac{\Delta y}{\Delta x} \right)$$

$$\tilde{x} = \frac{(y_{k,JL-1} - y_{i,JL} + x_{i,JL} \tan \theta - x_{k,JL-1} \tan \Psi)}{(\tan \theta - \tan \Psi)}$$

$$\tilde{y} = y_{i,JL} + \tan \theta (\tilde{x} - x_{i,JL}).$$

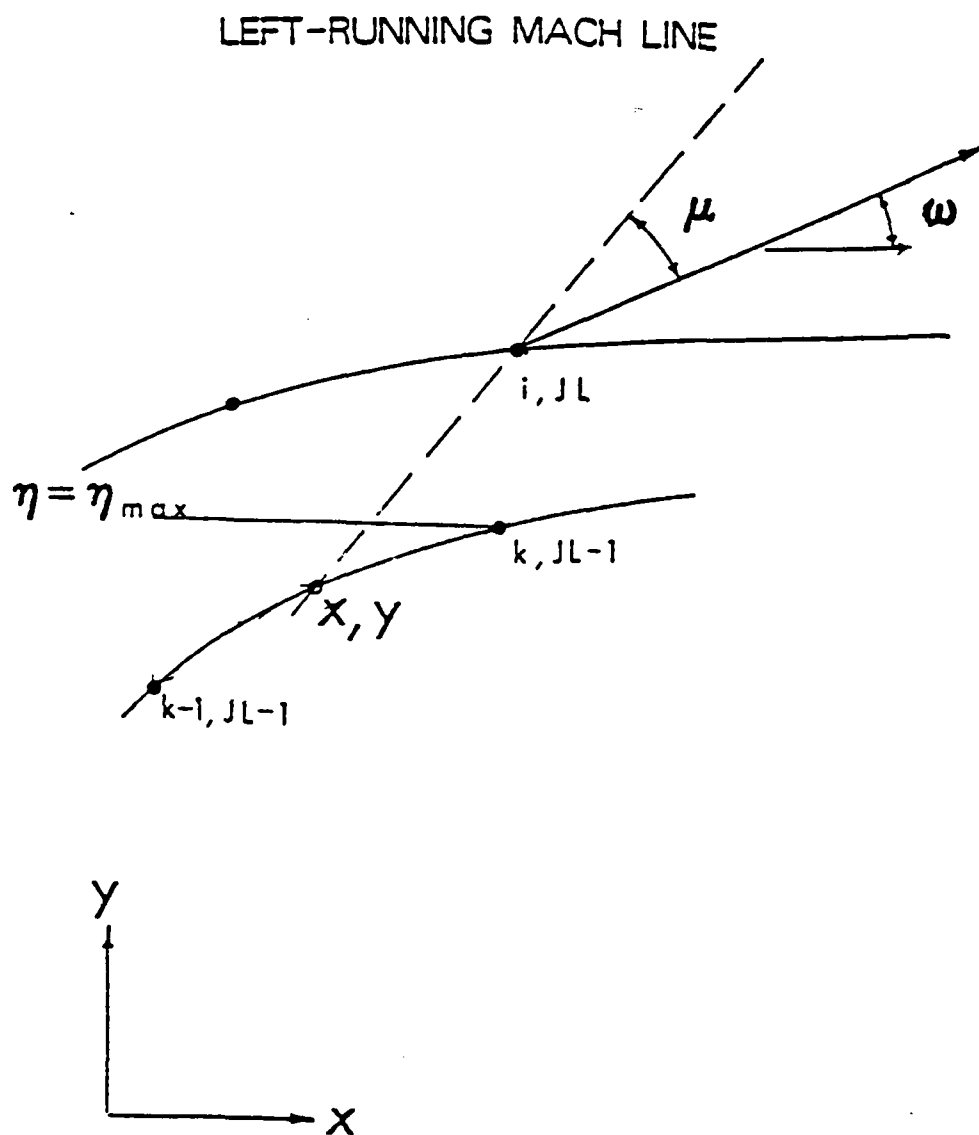


Figure A1. Non-reflection boundary condition.

INTENTIONALLY LEFT BLANK.

	<u>No of Copies</u>	<u>Organization</u>		<u>No of Copies</u>	<u>Organization</u>
(Unclass., unlimited)	12	Administrator		1	Commander
(Unclass., limited)	2	Defense Technical Info Center			US Army Missile Command
(Classified)	2	ATTN: DTIC-DDA			ATTN: AMSMI-RD-CS-R (DOC)
		Cameron Station			Redstone Arsenal, AL 35898-5010
		Alexandria, VA 22304-6145		1	Commander
	1	HQDA (SARD-TR)			US Army Tank Automotive Command
		WASH DC 20310-0001			ATTN: AMSTA-TSL (Technical Library)
					Warren, MI 48397-5000
	1	Commander		1	Director
		US Army Materiel Command			US Army TRADOC Analysis Command
		ATTN: AMCDRA-ST			ATTN: ATAA-SL
		5001 Eisenhower Avenue			White Sands Missile Range, NM 88002-5502
		Alexandria, VA 22333-0001			
	1	Commander	(Class. only)	1	Commandant
		US Army Laboratory Command			US Army Infantry School
		ATTN: AMSLC-DL			ATTN: ATSH-CD (Security Mgr.)
		Adelphi, MD 20783-1145			Fort Benning, GA 31905-5660
	2	Commander	(Unclass. only)	1	Commandant
		Armament RD&E Center			US Army Infantry School
		US Army AMCCOM			ATTN: ATSH-CD-CSO-OR
		ATTN: SMCAR-MSI			Fort Benning, GA 31905-5660
		Picatinny Arsenal, NJ 07806-5000			
	2	Commander	(Class. only)	1	The Rand Corporation
		Armament RD&E Center			P.O. Box 2138
		US Army AMCCOM			Santa Monica, CA 90401-2138
		ATTN: SMCAR-TDC		1	Air Force Armament Laboratory
		Picatinny Arsenal, NJ 07806-5000			ATTN: AFATL/DLODL
	1	Director			Eglin AFB, FL 32542-5000
		Benet Weapons Laboratory			<u>Aberdeen Proving Ground</u>
		Armament RD&E Center			Dir, USAMSAA
		US Army AMCCOM			ATTN: AMXSY-D
		ATTN: SMCAR-LCB-TL			AMXSY-MP, H. Cohen
		Watervliet, NY 12189-4050			Cdr, USATECOM
	1	Commander			ATTN: AMSTE-TO-F
		US Army Armament, Munitions			Cdr, CRDEC, AMCCOM
		and Chemical Command			ATTN: SMCCR-RSP-A
		ATTN: SMCAR-ESP-L			SMCCR-MU
		Rock Island, IL 61299-5000			SMCCR-MSI
	1	Commander			Dir, VLAMO
		US Army Aviation Systems Command			ATTN: AMSLC-VL-D
		ATTN: AMSAV-DACL			
		4300 Goodfellow Blvd.			
		St. Louis, MO 63120-1798			
	1	Director			
		US Army Aviation Research			
		and Technology Activity			
		Ames Research Center			
		Moffett Field, CA 94035-1099			

<u>No. of Copies</u>	<u>Organization</u>
7	<p>Commander US Army AMCCOM ATTN: SMCAR-LCA-F/Kline Flemming Kahn Hudgins SMCAR-CCL-CA/Hirlinger O'Neill Miller Picatinny Arsenal, NJ 07806-5000</p>
2	<p>Commander David W. Taylor Naval Ship ATTN: Dr. S. de los Santos Mr. Stanley Gottlieb Bethesda, MD 20084-5000</p>
2	<p>Commander US Naval Surface Weapons Center ATTN: Code DK20/Clare Moore Dahlgren, VA 22448-5000</p>
2	<p>Sandia National Laboratories ATTN: Dr. W.L. Oberkampf Dr. F. Blottner Division 1636 P.O. Box 5800 Albuquerque, NM 87185</p>
1	<p>Massachusetts Institute of Technology ATTN: Tech Library 77 Massachusetts Avenue Cambridge, MA 02139</p>
3	<p>Director NASA Ames Research Center ATTN: MS-202-1, Dr. T. Pulliam MS-258-1, Dr. J. Steger Dr. L. Schiff Moffett Field, CA 94035</p>
1	<p>Virginia Polytechnic Institute & State University P.O. Box 50 Blacksburg, VA 24061</p>

<u>No. of Copies</u>	<u>Organization</u>
1	<p>Commandant USAFAS ATTN: ATSF-TSM-CN Fort Sill, OK 73503-5600</p>
2	<p>Ford Aerospace and Communications Corporation Aeronautic Division ATTN: Charles White Bud Blair Ford Road Newpoint Beach, CA 92658</p>
2	<p>Honeywell Incorporation ATTN: Wilford E. Martwick Ken Sundeen 600 Second Street, North East Hopkins, MN 55343</p>
1	<p>NASA, Langley Research Center Transonic Aerodynamics Division ATTN: Dr. Michael J. Hemsch Hampton, VA 23665</p>
1	<p>Applied Technology Associates ATTN: Mr. R.J. Cavalleri P.O. Box 19434 Orlando, FL 32814</p>
1	<p>United States Military Academy Department of Mechanics ATTN: LTC Andrew L. Dull West Point, NY 10996</p>